Capillarity
Vol. 18, No. 2, p. 68-82, 2026

Original article

Pore-scale investigation of brine evaporation and salt precipitation in fractured porous media

Wilson Susanto[1]*, Muhammad Nasir[1], Bowen Wang[1], Sotheavuth Sin[1], Anindityo Patmonoaji[2], Shintaro Matsushita[1], Tetsuya Suekane[1]

[1]*Department of Mechanical Engineering, Institute of Science Tokyo, Tokyo 1528550, Japan*
[2]*Department of Chemical Engineering, University College London, WC1E 7JE, United Kingdom*

Keywords:
Fractured porous media
salt precipitation
capillary backflow
evaporation
capillarity
X-ray microtomography

Cited as:
Susanto, W., Nasir, M., Wang, B., Sin, S., Patmonoaji, A., Matsushita, S., Suekane, T. Pore-scale investigation of brine evaporation and salt precipitation in fractured porous media. Capillarity, 2026, 18(2): 68-82.
https://doi.org/10.46690/capi.2026.02.03

Abstract:
Understanding salt precipitation during evaporation in fractured porous media is essential for predicting pore-structure evolution, fracture permeability changes, and leakage mitigation. In fractured systems, brine transport occurs in both fracture and matrix domains, resulting in complex interactions. Using X-ray microtomography, this study investigated the mechanisms of brine evaporation and salt precipitation in such media. The results revealed two distinct stages of salt migration: (I) Evaporation and capillary transport, and (II) salt precipitation and accumulation. In Stage I, fractures acted as preferential gas pathways, exhibiting lower brine saturation, while the matrix retained higher saturation due to stronger capillarity. Residual brine films on particle surfaces within the fracture sustained evaporation and enabled capillary backflow from the matrix, further increasing brine concentration. In Stage II, once solubility limits were exceeded, salt crystals formed in the fracture, inducing additional capillary suction that drew more brine from the matrix and promoted further salt deposition. Increasing the gas flow rate limited brine migration toward the fracture center, thereby reducing salt accumulation in the fracture. At low flow rates, capillary replenishment from the matrix dominated over evaporation, sustaining continuous brine supply and extensive salt deposition throughout the fracture. At high flow rates, evaporation prevailed, restricting brine transport and confining salt accumulation mainly to the fracture-matrix interface. Across all conditions, salt precipitation progressively reduced effective pore sizes in both fracture and matrix, with implications for fracture permeability evolution.

1. Introduction

Geological storage of CO_2 in saline aquifers through underground injection is recognized as a crucial technology for reducing greenhouse gas emissions and supporting global carbon neutrality targets (Bachu, 2008; IPCC, 2022). During CO_2 injection, evaporation of brine can induce salt precipitation, progressively alter pore structures, and reduce permeability within porous media, reducing injectivity or storage performance (Ott et al., 2011; Miri et al., 2016; Sun et al., 2025). The degree of permeability reduction is strongly affected by both the spatial pattern and spatial distribution of salt (Pruess and Müller, 2009; Zhang and Liu, 2016; Grimm Lima et al., 2020). Therefore, the elucidation of precipitation mechanisms is essential for predicting reservoir performance and mitigating risks of injectivity loss or leakage.

Salt migration during gas injection involves displacement

---

*Corresponding author.
E-mail address: wilson.susanto@mail.ugm.ac.id (W. Susanto); muh.nasir.aa@gmail.com (M. Nasir); wang.b.al@m.titech.ac.jp (B. Wang); ssotheavuthsin@gmail.com (S. Sin); a.patmonoaji@ucl.ac.uk (A. Patmonoaji).

Received October 3, 2025; revised November 16, 2025; accepted December 11, 2025; available online December 15, 2025.

Yandy Scientific Press

and subsequent evaporation (Raats, 1973; Wu et al., 2020; Yan et al., 2025). During displacement, the injected gas pushes brine within the porous structure, redistributing liquid and defining the initial saturation and connectivity of water films (Suekane et al., 2015; Hu et al., 2020). After the occurrence of displacement, water evaporation increase local salt concentration inducing concentration gradients, capillary backflow resulting from capillary pressure gradient, and diffusive transport (Miri et al., 2015; Akindipe et al., 2021; Chen et al., 2024). Salt redistribution and crystallization predominantly occur during evaporation, governing the spatial pattern of precipitation (Shahidzadeh et al., 2015; Sun et al., 2025). Therefore, the location of precipitation within the context of evaporation-driven processes induced by gas injection was observed herein.

Evaporation-driven precipitation within porous media is fundamentally governed by the interplay between evaporation rate, surface area, and pore connectivity (Raats, 1973; Shokri et al., 2010; Shokri, 2014). The evaporation rate is influenced by the gas velocity, vapor pressure difference, and temperature gradient, which together determine the rate of liquid-to-vapor mass transfer across the interface. Under gas injection, the injected gas advects vapor through the pore space, and the evaporation flux can be approximated by the relation:

$$J_v \propto Q_g \left(C_{v,s} - C_{v,out}\right) \tag{1}$$

where J_v is the evaporation flux (kg/m^{2}s), Q_g is the gas injection rate (m^3/s), and $C_{v,s}$ and $C_{v,out}$ represent the vapor concentrations at the interface and the outlet (kg/m^3), respectively (Dashtian et al., 2018; He et al., 2019). Hydraulic connectivity governs capillary replenishment, allowing liquid migration from saturated to drying regions, thereby controlling the temporal evolution of saturation and salt distribution (Miri et al., 2015; Akindipe et al., 2021; Chen et al., 2024; Susanto et al., 2025). In such systems, conventional dimensionless parameters such as the capillary number (Ca) and the Péclet number (*Pe*) are not directly applicable. The Ca becomes irrelevant after two-phase breakthrough, as the system transitions into a gas-dominated regime where viscous and capillary forces are no longer balanced (Miri et al., 2016). Similarly, the *Pe* number cannot consistently represent coupled gas-liquid transport, since it describes either gas advection or brine diffusion independently (Pruess and Müller, 2009; Zhang et al., 2020). In previous work, the evaporation rate and Darcy velocity of the liquid phase were analyzed to capture the interplay between evaporation and liquid transport within the porous medium. Although the velocity was derived from evaporation fluxes and saturation distributions rather than directly imposed, it provided insight into the transition between diffusion and advection dominated regimes during evaporation. Building upon this framework, the present study extends the investigation to a fracture-matrix porous system, where strong contrasts in pore structure and hydraulic connectivity introduce additional complexity in the coupling between evaporation, capillary backflow, and salt precipitation.

Evaporation-driven salt precipitation in fractured porous media is highly complex because of the pronounced heterogeneity between fracture apertures and surrounding matrix pores (Dashtian et al., 2018; Roy, 2022). Previous studies have successfully identified the spatial distribution of salt deposition and the locations of active evaporation fronts within fractures (Ott et al., 2011; Chen et al., 2024). However, the underlying liquid transport mechanisms, particularly the coexistence of capillary flow toward the fracture and capillary backflow from the matrix, remain difficult to quantify and interpret (Bogdanov et al., 2003; Pruess and Müller, 2009; Zhang et al., 2020). These coupled processes are strongly influenced by the gas injection rate, which governs the balance between evaporation and capillary replenishment, leading to variable salt accumulation patterns and fracture evolution (Miri et al., 2016; He et al., 2019). In this study, both evaporation-induced capillary flow and compensating backflow are differentiated within a unified pore-scale framework through experiments performed under varying gas flow conditions.

To differentiate the liquid transport processes, a salt-tracking approach based on high-resolution X-ray microtomography (micro-CT) was employed. Pore-scale characterization of these coupled phenomena is challenging because it requires simultaneous imaging of evaporation fronts, brine migration, and salt redistribution. Micro-CT enables non-destructive visualization of such dynamics and has been widely applied to study pore-scale fluid and salt transport (Shokri et al., 2010; Shokri, 2014; Bultreys et al., 2016). In our previous work, this technique was used to quantify salt minerals through brine concentration and saturation measurements, allowing direct observation of mineral redistribution and precipitation within the pore space (Sin et al., 2024; Susanto et al., 2025). Building on that framework, the present study extends the analysis to a fracture-matrix system, where simultaneous tracking of salt redistribution and estimation of liquid-phase flow enables clear differentiation between evaporation-induced capillary flow and compensating backflow within a unified pore-scale framework. Furthermore, the corresponding changes in pore size and porosity were quantified to evaluate their influence on permeability. This integrated approach provides new insight into the coupled mechanisms that govern salt accumulation and self-sealing behavior in fractured porous media under varying gas injection conditions.

Using micro-CT, we investigated the pore-scale mechanisms of salt precipitation in a fracture-matrix porous system under continuous gas injection, additionally exploring the effects of gas injection flow rate on brine redistribution and capillary backflow. The materials used in the experimental setup, procedures, and employed image processing methods are described in the following section. Section 3 presents the data analysis, including the pore-scale evolution of brine-salt phases, the effect of flow rate on mass transfer, and the implications of salt accumulation for the properties of the fracture and porous media. Section 4 concludes the study by summarizing key findings and implications for the elucidation of fracture-matrix dynamics during gas-induced salt precipitation.

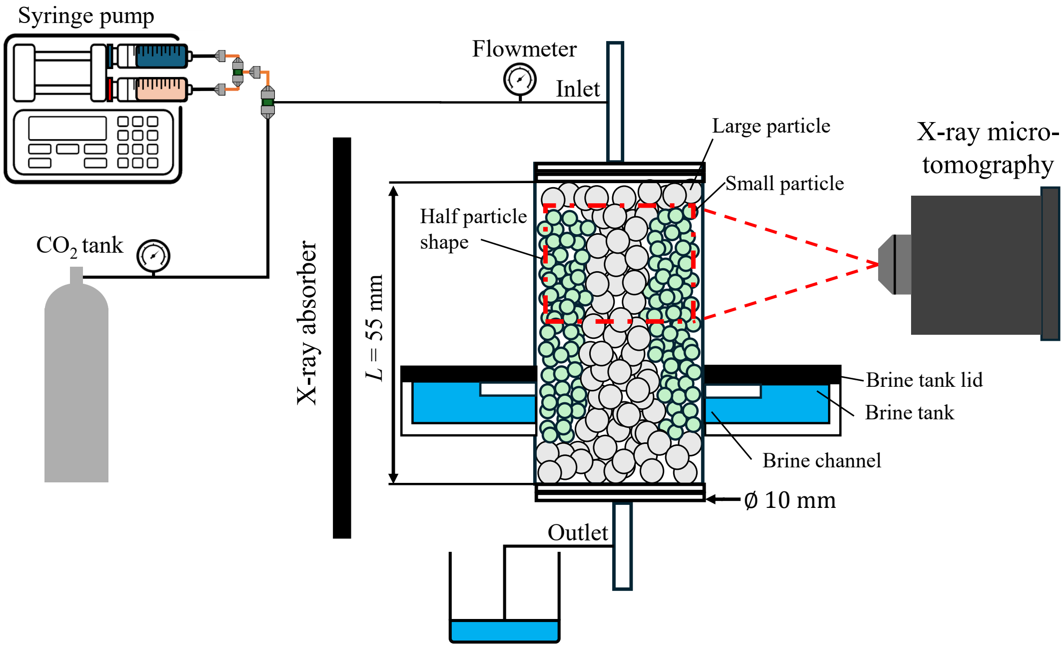

Fig. 1. Schematic of the three-dimensional experimental setup for examining brine evaporation and salt precipitation mechanisms.

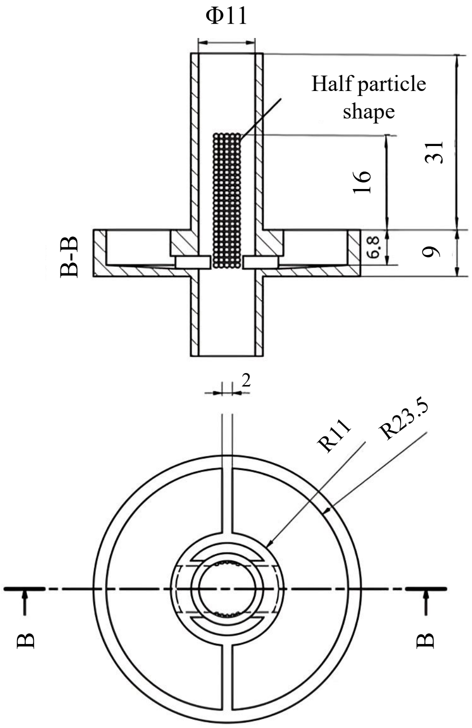

Fig. 2. Engineering drawing of the packed-bed main body, showing the brine supply tank, connecting channel, and a half-cut cross-section of the internal structure and fracture area.

2. Material and methods

Three-dimensional (3D) experiments were conducted to investigate brine evaporation and salt precipitation in brine-supplied fractured porous media using a custom-designed experimental setup (Fig. 1). All experiments were performed at room temperature (∼ 25 °C) and atmospheric pressure, with CO_2 used as the injection gas.

2.1 Experimental setup

The packed bed container consisted of four pieces 3D-printed components fabricated using an SLA 3D printer (Formlabs, Somerville, MA, USA): An inlet, a cylindrical main body, a supply tank lid, and an outlet (Patmonoaji et al., 2022). The main body dimensions are shown in Fig. 2. A brine supply tank with a capacity of 6,524 mm^3 is attached 15 mm above the outlet, directly connected to the interior of the porous media to continuously replenish brine during injection. Two water-wet glass beads (As One, BZ-O6) with diameters of 400 and 1,000 µm were used. Their combination ensured immobility during gas injection while providing a controlled fracture-matrix structure (Kézdi, 2013).

During sample preparation, the outlet was installed into the main body, and a 5-mm-thick bottom layer of 1,000-µm beads was added to isolate the smaller beads from the outlet boundary. A separator was then inserted, and a second layer of 1,000-µm beads was placed in the column center to create an artificial fracture zone. The surrounding regions were packed with 400-µm beads to represent the matrix. Continuous shaking during filling promoted random close packing and minimized heterogeneity (Bernal and Mason, 1960). Finally, a thin layer of 1,000-µm beads was placed near the inlet to separate the two matrix domains. This configuration produced a controlled fracture-matrix structure with an estimated volume ratio of matrix-left: Fracture: Matrix-right ≈ 1:1.8:1 and a total pore volume of 759 mm^3. The packed bed was then closed with the top injection module, yielding a packing height (L)

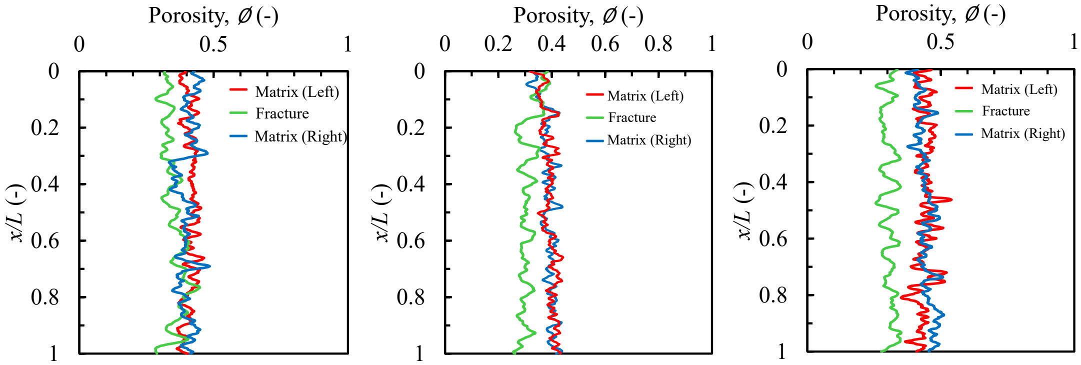

(a) (b) (c)

Fig. 3. Porosity distributions for the fracture and matrix along the packed bed as functions of normalized vertical position (x/L), where x is the vertical location and L is the total observed length.

Table 1. Permeability estimation in the matrix and fracture regions at three different flow rates.

Case	Injection rate (cm^3/min)	Permeability (mD)		
		Matrix (left)	Fracture	Matrix (right)
1	30	0.1190	0.0980	0.1100
2	50	0.0946	0.0820	0.0880
3	80	0.0960	0.0687	0.1300

of 55 mm. Brine drying was monitored using a micro-CT scanner (Comscantechno, ScanXmate-CF110TSS300) during CO_2 injection. The micro-CT observation region ($11.4 \times 11.4 \times 10.8$ mm^3) was located 5 mm below the injection point. The careful bead packing ensured negligible particle displacement during gas injection, providing stable and reproducible experimental conditions. To suppress wall effects and prevent preferential gas flow along the container wall, half-spherical beads with the same diameter as the packing particles were fixed to the inner wall surface.

2.2 Capillary rise and permeability estimation

To confirm that capillary forces were sufficient to supply brine from the reservoir to the observation region, the capillary rise height (h) was estimated as:

$$h = \frac{2\gamma\cos\theta}{\rho_0\rho_L g r_e} \tag{2}$$

where γ is the liquid-air surface tension (N/m), θ is the contact angle, ρ_0 is initial brine density (kg/m^3), g is the gravitational acceleration (m/s^2), and r_e is the effective pore radius (m). For the 400-μm beads, the calculated capillary rise is approximately 123-157 mm. This range reflects the changes in density and surface tension during evaporation. The estimated height is sufficient to supply liquid to the region of interest, located 24 mm above the reservoir.

For each experimental case, the permeability was estimated from the porosity and the average pore diameter listed in Table 1, where the fracture area has less permeability compared to the matrix area. The calculation was performed using the Kozeny-Carman equation:

$$k = \frac{d^2\emptyset^3}{180\left(1-\emptyset\right)^2} \tag{3}$$

where d is the particle diameter and $\emptyset$ is the porosity of the packed bed. Based on the average permeabilities for cases 1-3 is $k_1 = 0.109$ mD, $k_2 = 0.0828$ mD, and $k_3 = 0.0982$ mD, respectively. To quantify potential brine replenishment into the matrix, the permeability k of the 400-μm bead matrix was also measured using Eq. (3). The capillary pressure was calculated as:

$$P_c = 0.866\ x\frac{2\gamma\cos\theta}{d^2} \tag{4}$$

where P_c is the capillary pressure (kg/(m·s^2)), the factor 0.866 accounts for the pore-throat geometry of a tetrahedral packing of spheres. The corresponding capillary-driven Darcy velocity was estimated as:

$$v_c = \frac{kP_c}{\mu L} \tag{5}$$

where μ is the dynamic viscosity of brine (kg/(m·s)), and L is the characteristic length of the matrix region (m). Using this approach, the maximum capillary velocity was calculated as 0.02 m/s, sufficient to refill the matrix under experimental conditions. The calculated 0.02 m/s is a theoretical maximum under ideal 1D conditions. However, because of tortuosity and pore-scale resistance, effective capillary-driven velocities are typically two to three orders of magnitude smaller (10^{-6}-10^{-5} m/s) in glass-bead and sandstone systems (Blunt, 2017). Based on these realistic velocities, the minimum time required for brine to fully occupy the pore space, and thus for evaporation to proceed, is approximately 12 h.

2.3 Experimental procedures

Prior to each experiment, CO_2 was briefly injected to verify the absence of blockage in the artificial fracture. The packed bed was then scanned using micro-CT to determine porosity and pore-size distributions (Figs. 3 and 4). Although minor

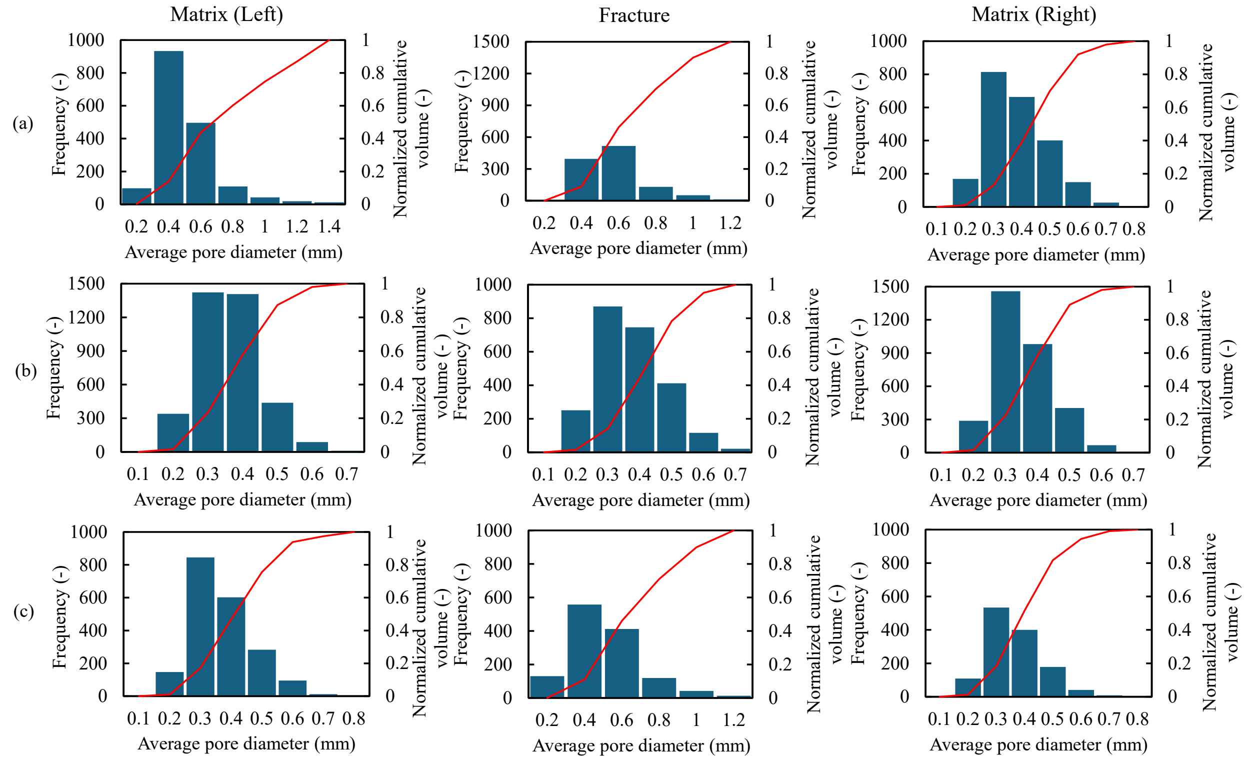

Fig. 4. Pore-size distribution in the matrix and fracture regions of the fractured porous media under initial conditions, expressed in terms of frequency and normalized cumulative volume. The results indicate spatial variations in pore structure prior to gas injection at flow rates of (a) 30, (b) 50, and (c) 80 cm^3/min.

Table 2. Experimental conditions in the observed region of the packed bed.

Case	Injection rate(cm^3/min)	Initial porosity (%)			Average pore-size distribution (mm)		
		Matrix	Fracture	Matrix	Matrix	Fracture	Matrix
1	30	41 ± 2	35 ± 3	40 ± 3	0.38	0.41	0.37
2	50	38 ± 3	31 ± 3	39 ± 2	0.37	0.48	0.37
3	80	40 ± 4	32 ± 3	42 ± 3	0.35	0.41	0.35

differences in pore structure exist between cases, the overall porosity and pore-size distributions were verified with error of ±10%-15%, ensuring comparable permeability characteristics across all experiments. Micro-CT analysis was performed on three distinct regions, associated with the left matrix, fracture, and right matrix domains. The detailed distribution of porosity along the packed bed is provided in Fig. 3. Average porosities were 40% ± 2% for the matrices and 33% ± 3% for the fractures. The lower porosity in the fracture domains was attributed to the small 400-µm beads penetrating the fracture pore throats during packing, which locally reduced the void fraction. Additionally, the pore-size distributions are shown in Fig. 4 exhibit a uniform, single-peak distribution. Experimental conditions, initial average porosity, and average pore-size distribution in the observed region of the packed bed are summarized in Table 2.

A sodium iodide (NaI) solution with a concentration (C) of 20 wt% (0.25 g/cm^3) was used as a brine, with a solubility limit of 64 wt% at 20 °C (Seidell, 1928). Throughout the experiments, brine concentration (mass fraction of NaI) was monitored to track water loss and salt precipitation. NaI was selected because of its X-ray attenuation properties, providing sufficient phase contrast in micro-CT imaging, consistent with our previous work (Susanto et al., 2025). Density-grayscale calibration details are provided in Fig. S1. To fully saturate the packed bed with water, the supply tank was first filled with brine and closed. The packed bed was then partially submerged in liquid within a vacuum chamber to ensure thorough saturation. During vacuuming, air inside the porous medium was displaced with the liquid for over 30 min, leaving the column under vacuum. Once bubble formation ceased, atmospheric pressure was restored, forcing the liquid into the column to attain full saturation (Patmonoaji et al., 2020).

The packed bed was placed inside the micro-CT scanner, with the X-ray tube set to a voltage of 100 kV and a current of 100 µA. Imaging was performed with 2,400 projections and

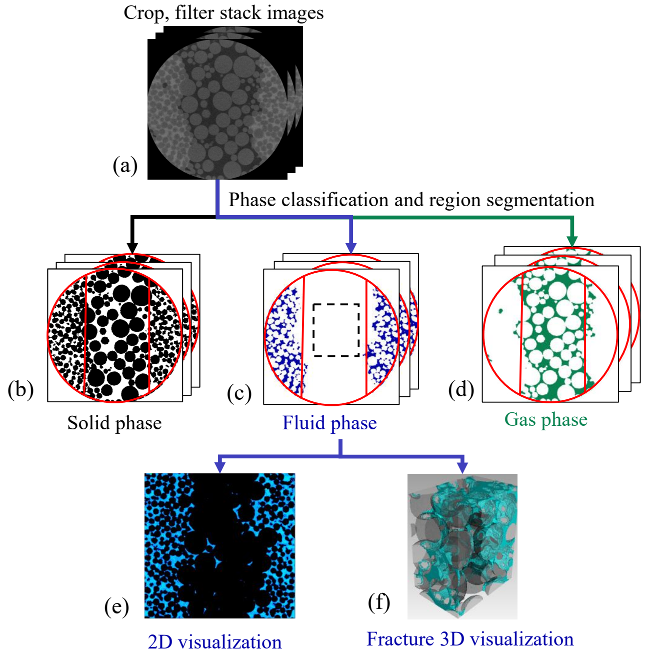

Fig. 5. Image processing workflow: (a) Cropped filtered stack image captured using micro-CT, (b) segmented solid phase, (c) segmented fluid phase, (d) segmented gas phase, (e) two-dimensional visualization of fluid distribution, and (f) 3D visualization of fluid distribution in the fracture.

a voxel size of 10 μm/pixel. The scanning time was 40 min, with gas injection halted during scanning. As salt movement is primarily driven by evaporation, drainage was conducted under the same conditions to achieve the target trapped brine saturation. CO_2 was then injected downward into the fully saturated packed bed using a syringe pump at a constant flow rate of 25 cm^3/min for 96 s. The corresponding Ca was on the order of 1×10^{-7}, indicating capillary-dominated displacement (Joekar-Niasar and Hassanizadeh, 2012), which was quantified to characterize the initial brine redistribution. While CO_2 partially displaced brine in the fracture, the brine within the matrix remained fully connected. This setup ensured that brine would be available for subsequent evaporation and salt precipitation analyses.

2.4 Image processing

The scanned data was reconstructed using the ConeCTExpress software (Comscantechno). Fig. 5 presents the image processing workflow used to obtain the phase distribution and concentration inside the porous media, with particular emphasis on brine and gas fractions relevant to evaporation and capillary backflow. All data processing was performed using the FIJI software (Schindelin et al., 2012), with the filtered image shown in Fig. 5(a). To improve the clarity and focus of the images, we applied ring artifact correction, noise removal, and beam-hardening filters. To minimize beam-hardening side effects, the field of view was narrowed to 952 pixels, corresponding to ~ 9.5 mm in diameter. In addition, approximately 50 slices at both the top and bottom of each scan were excluded because of poor image quality caused by cone-beam effects. Median and non-local mean denoising filters were subsequently applied to further reduce noise (Wang et al., 2018).

Binarization separated the solid (Fig. 5(b)), fluid (Fig. 5(c)), and gas (Fig. 5(d)) phases, which were then stacked to reconstruct two-dimensional and 3D images. Porosity was quantified from the solid fraction, and pore-size distribution was determined using a watershed segmentation algorithm (Gostick, 2017). A vertical cross-section of the brine during drying is shown in Fig. 5(e). At the pore scale, salt precipitation was observed in the fracture region (black rectangular strip), particularly within a central volume of 4.1 × 2.8 × 5.4 mm^3 (Fig. 5(f)), which was analyzed to elucidate the mechanism and pattern of salt deposition.

To determine the area of the gas-liquid interface, a two-pixel dilation was applied to the binary gas-phase images. The overlap between the dilated gas and liquid phases was then extracted using a Boolean "AND" operation in ImageJ (Hu et al., 2020; Nasir et al., 2022). Any intersections coinciding with the solid phase were removed, leaving only the true gas-liquid interface. The resulting overlap in each cross-sectional slice represents the local interfacial area.

3. Results and discussion

3.1 Evolution of brine redistribution and salt precipitation

Pore-scale visualization was conducted to elucidate the mechanisms of salt precipitation induced by brine evaporation. Fig. 6 illustrates pore-scale brine evaporation in a three-dimensional fractured porous medium, observed 5 mm below the inlet under low and high gas flow rates. The color scale represents brine concentration, while black regions indicate solid particles and gas-filled pores. The purple color denotes the gas phase; however, during the dry-out stage, the gas phase is rendered in black together with the solid particles. Time 0 h corresponds to the onset of evaporation, followed by continuous gas injection. The vertical cross-sectional concentration distribution highlights the progressive increase in brine concentration and ultimately transitions into precipitated salt. The drying process was qualitatively divided into two stages based on brine concentration. Stage I corresponds to the evaporation stage, during which brine concentration increases due to water loss, without visible salt formation, sustained by capillary flow in the matrix. Stage II corresponds to the dry-out stage, characterized by rapid salt precipitation and the onset of salt-induced capillary suction once supersaturation is exceeded. Figs. 7 and 8 provide quantitative measurements of cross-section-averaged brine saturation and brine concentration in the fracture and matrix regions, allowing the detailed examination of salt migration and accumulation over time. At the medium flow rate, the same two-stage mechanism was observed; thus, the relevant results are provided in Fig. S2 for the main text to focus on low and high flow rates as representative cases. Together, Figs. 6-8 illustrate the interplay of evaporation, capillary backflow, and salt precipitation within the fracture-matrix system.

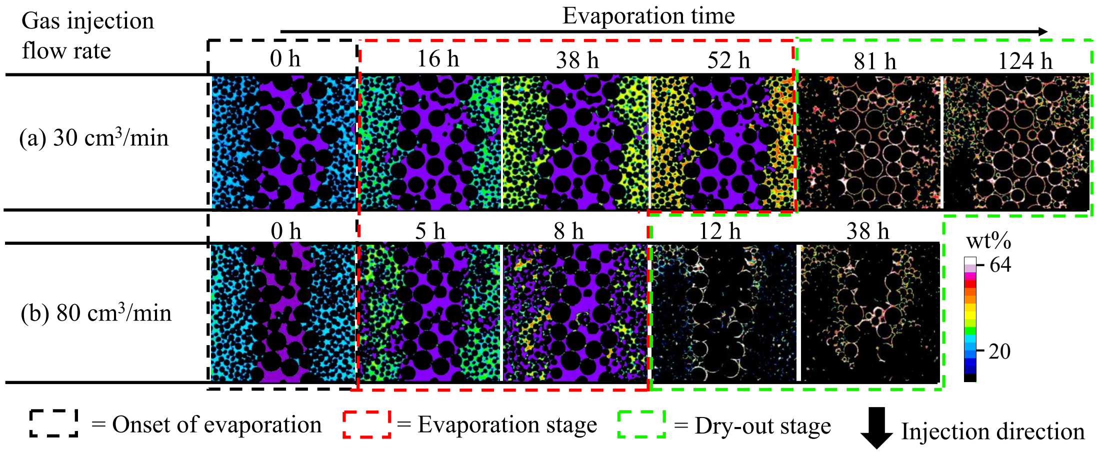

Fig. 6. Concentration distribution of trapped brine and corresponding salt precipitation in fractured porous media, visualized through vertical cross-sections at (a) low and (b) high flow rates (30 and 80 cm^3/min, respectively).

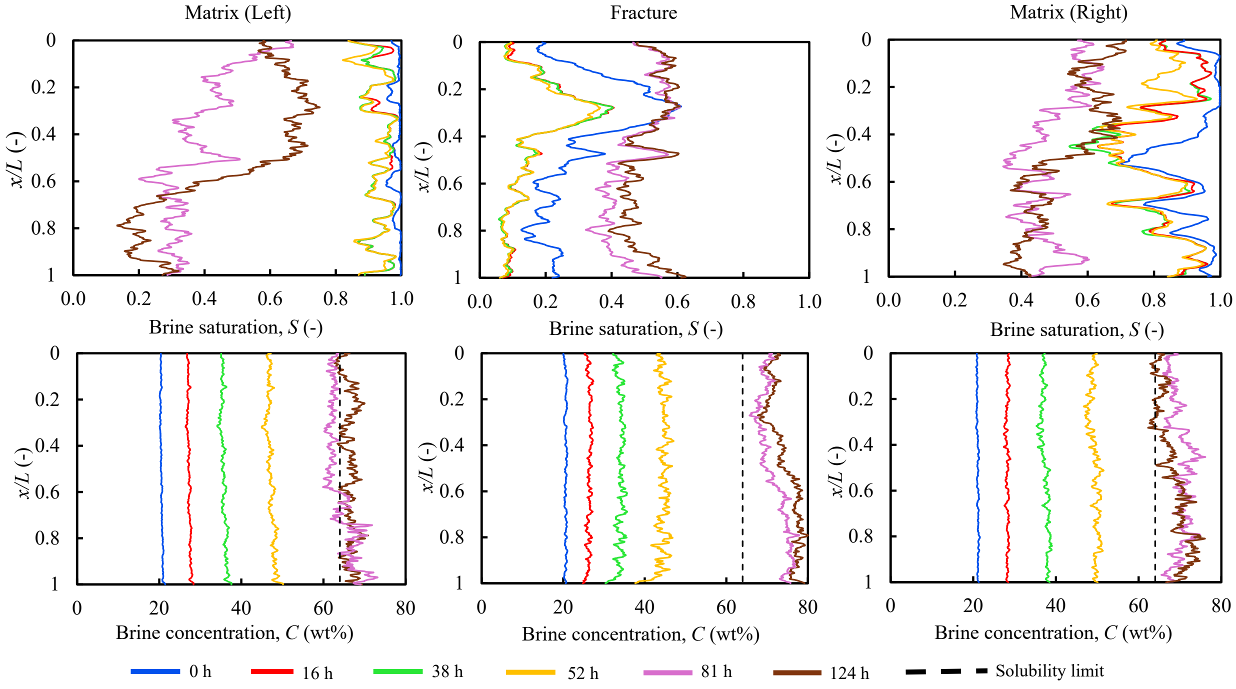

Fig. 7. Profiles of slice-averaged brine saturation and brine concentration along the normalized sample height (x/L) at an injection rate of 30 cm^3/min. Where x is the vertical location and L is the total observed length.

At the onset of gas injection, the gas preferentially invaded the fracture because of its larger pore size and lower flow resistance, whereas brine remained trapped in the smaller matrix pores under stronger capillary forces (Fig. 6). Because the matrix exhibits strong capillarity and the fracture is directly exposed to CO$_2$, the evaporation front formed naturally at or near the fracture-matrix interface. Although brine in the fracture was partially displaced, the average saturation remained 0.20-0.25 (Figs. 7 and 8), with brine persisting as a thin film on particle surfaces owing to the water-wet nature of the medium (Zhao et al., 2016; Nasir et al., 2022; Yan et al., 2025). These water films maintained liquid connectivity, enabling continued evaporation and capillary-driven brine transport. As evaporation progressed, brine transported from the matrix via capillary backflow increasingly concentrated in the fracture. This resulted in the formation of a concentrated evaporation zone at the fracture center, where local brine concentration was highest and supersaturation triggered preferential salt precipitation. The onset of the evaporation stage was marked by a uniform increase in brine concentration along the fracture and matrix profiles. Brine saturation in the fracture decreased to 0.1 at both flow rates. The residual brine, being directly exposed to CO$_2$, underwent predominantly evaporation (Shahidzadeh-Bonn et al., 2008). In contrast, brine saturation in the matrix remained largely unchanged while brine concentration increased, indicating that capillary backflow at the fracture-matrix interface was sustained by capillary flow from the tank.

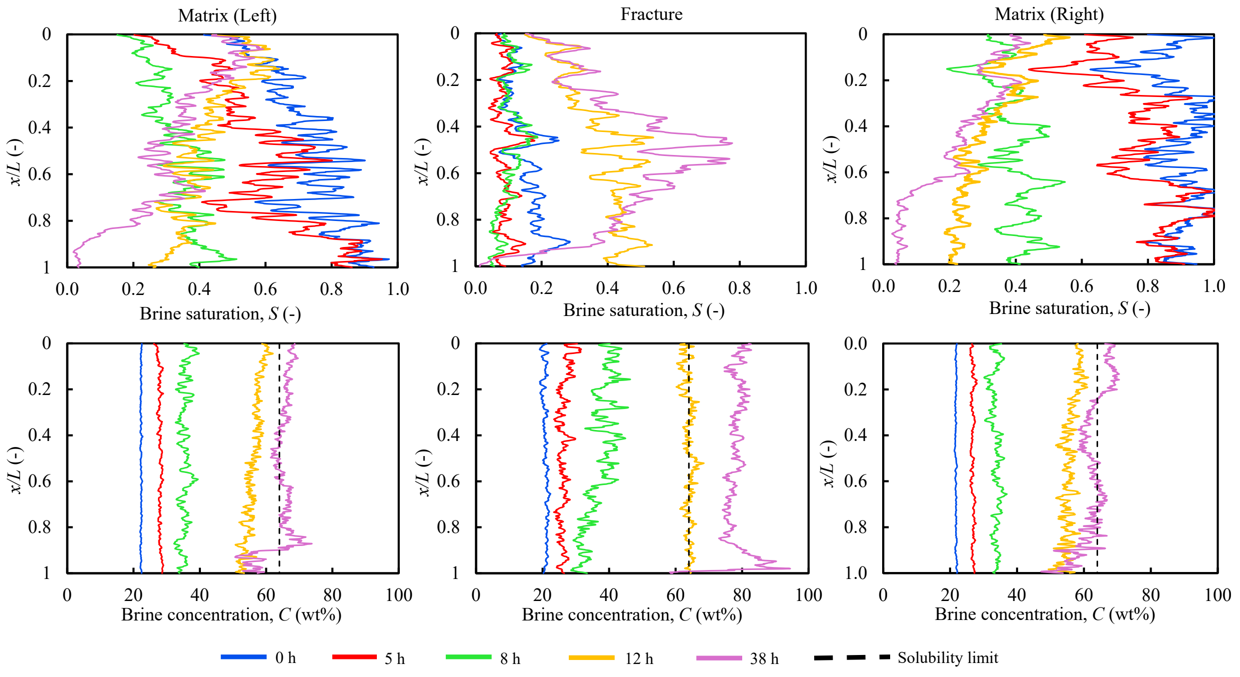

Fig. 8. Profiles of slice-averaged brine saturation and brine concentration at an injection rate of 80 cm^3/min.

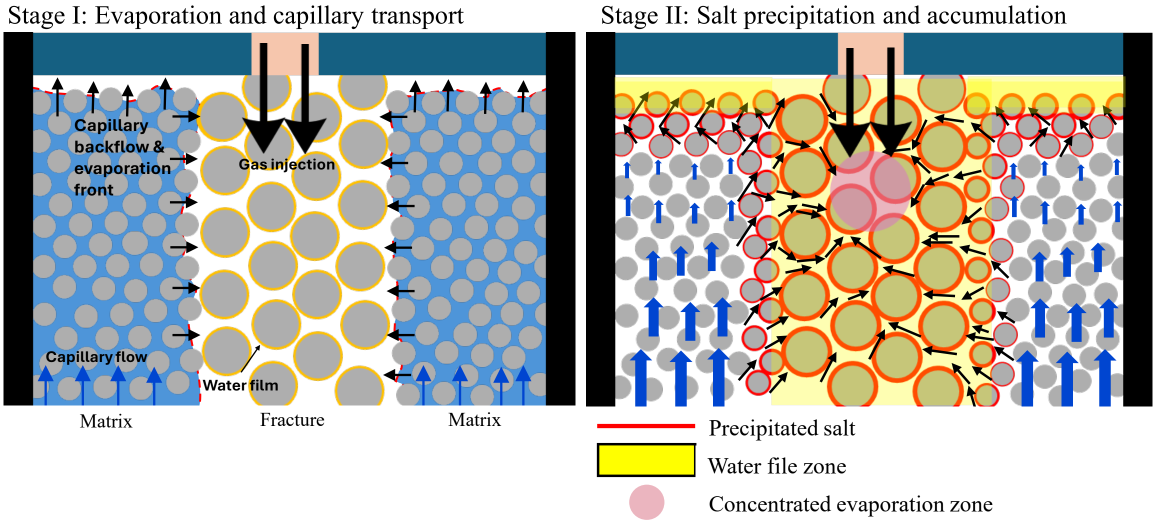

Fig. 9. Two-stage salt accumulation in a fractured porous medium induced by gas injection.

To clarify how salt precipitation develops after supersaturation, the spatial evolution of salt accumulation within the fracture–matrix system is examined. Once supersaturation is reached, salt preferentially precipitates at the fracture–matrix interface and subsequently progresses toward the region of concentrated evaporation (Fig. 6). Brine saturation increases along the profile and decreases in the matrix, indicating salt draw into the surrounding brine through the fracture-matrix interface, enhancing capillary backflow and accelerating accumulation in the fracture, as shown in the dry-out stage (Figs. 7 and 8). At both low and high flow rates during the dry-out stage, salt initially precipitates near the fracture-matrix interface and progressively aggregates toward the center of the fracture. The precipitated salt aligns along particle menisci, only partially obstructing the pores.

Based on pore-scale observations of brine redistribution and fracture-matrix interactions, the overall salt precipitation mechanism in fractured porous media can be divided into two stages (Fig. 9). In Stage I, evaporation at the front increases brine concentration while capillary backflow sustains liquid pathways in the fracture through the water film zone. A concentrated evaporation zone forms in the middle of the fracture, where the evaporation rate is the highest, driving a rapid increase in brine concentration. In Stage II, supersaturation triggers salt precipitation and growth at particle surfaces and high-evaporation zones, progressively reducing pore space and modifying transport. This two-stage mechanism indicates that evaporation, capillary backflow, and salt precipitation jointly

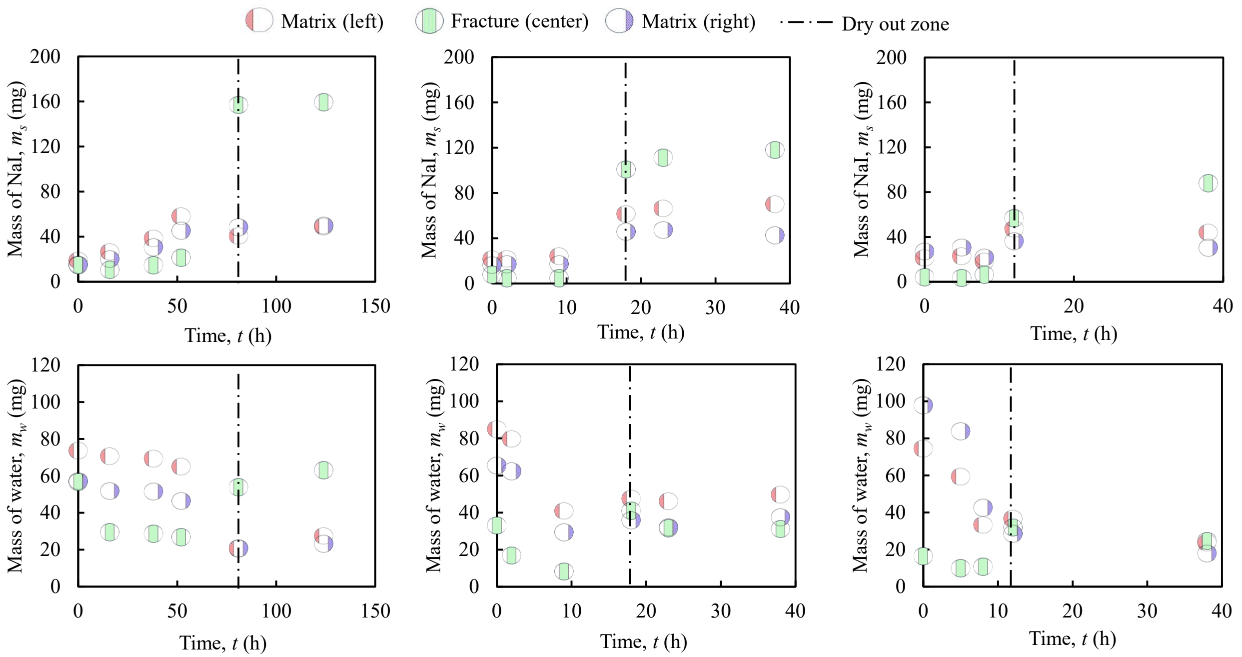

(a) (b) (c)

Fig. 10. Temporal evolution of water and NaI masses in the three regions (fracture and matrices) at flow rates of (a) 30, (b) 50, and (c) 80 cm^3/min. The dotted line marks the onset of dry-out.

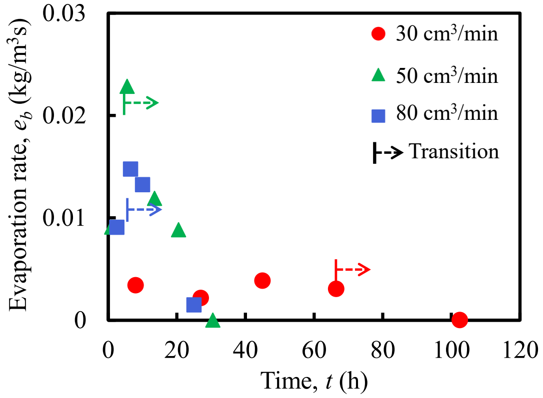

Fig. 11. Evaporation rate within the entire observed volume under three different flow rates. The arrow bars mark the brine reduction in matrixtle.

determine salt distribution. Although this mechanism is consistently observed in all experiments, the timing and spatial extension of salt precipitation toward the middle of the fracture strongly depend on the gas injection rate, which is discussed in the following section.

3.2 Effect of gas injection rate on salt precipitation dynamics

In this section, we discuss the effect of gas injection rate on salt precipitation by analyzing the mass transfer dynamics during gas injection into the brine-saturated porous medium. The primary mechanisms governing this process are evaporation at the gas-liquid interface and capillary backflow from the matrix to the fracture. To quantify evaporation, the mass of water lost was indirectly inferred from the local concentration of NaI in the brine (Norouzi Rad et al., 2013; Shokri, 2014). First, the contribution of capillary flow from the tank was estimated based on the increase in NaI mass in the system:

$$m_f = \frac{(\rho_t S_t x_t - \rho_{t-1} S_{t-1} x_{t-1})(1-C_t)}{x_t} \tag{6}$$

where m_f is the supplied water mass per bulk volume during the time step (kg/m^3); S_t and S_{t-1} are the average brine saturations at the current and previous time steps; ρ_t and ρ_{t-1} are the bulk brine densities (kg/m^3) at the current and previous time steps, respectively; and x_t and x_{t-1} are the corresponding NaI mass fractions in the brine. Using this approach, the effective bulk evaporation rate can then be estimated by combining the water mass reduction with additional water supplied via capillary flow:

$$e_b = \frac{S_{t-1}\rho_{t-1}(1-x_{t-1}) - S_t\rho_t(1-x_t) + m_f}{\Delta t} \tag{7}$$

where e_b is the effective bulk evaporation rate (kg/(m^3·s)); and Δt is the time interval between two consecutive scans (s). This method allows indirect determination of water loss based on the conservative tracer behavior in the brine, with brine concentration acting as a proxy for the change in water mass.

It should be noted that after salt precipitation, the measured mass of NaI may be overestimated. Micropore structures within the precipitated salt increase the apparent volume, which can exaggerate mass estimates derived from imaging. Despite this limitation, the data provides valuable insights into mass transfer trends and evaporation rates. Fig. 10 presents the total masses of NaI and water within the fracture and matrix domains, while the corresponding evaporation rate is shown in Fig. 11. At low flow rates, during 0-52 h, water mass decreases

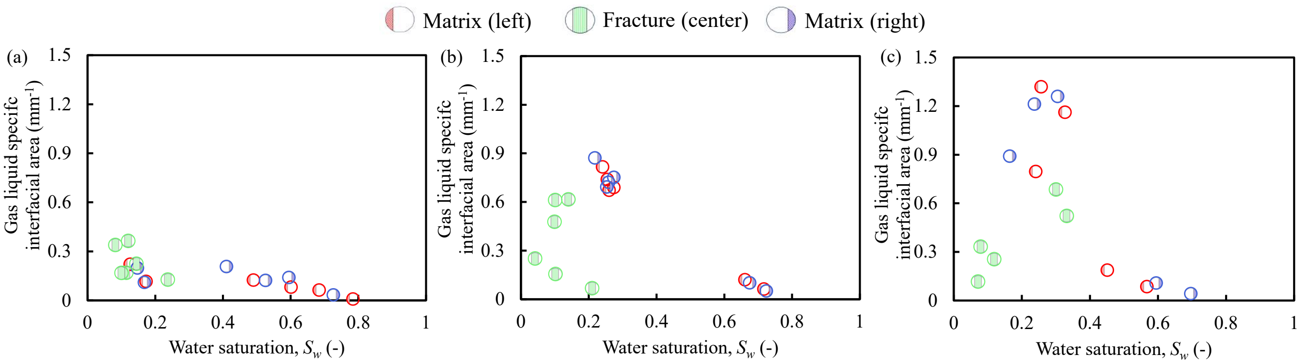

Fig. 12. Gas-liquid specific interfacial area in the matrix and fracture as a function of saturation, obtained from cross-sectional images at flow rates of (a) 30, (b) 50, and (c) 80 cm^3/min.

in both the matrix and fracture, with the fracture losing water faster due to direct exposure to CO_2. In the same period, the NaI mass in the matrix gradually increases, indicating that capillary flow from the tank replenishes the brine. Meanwhile, NaI in the fracture remains nearly constant until 38 h and increases slightly up to 52 h, reflecting the onset of brine capillary backflow into the fracture. The evaporation rate in Fig. 11 remains relatively steady from 0 to approximately 81 h but drops sharply afterward, as the highly concentrated brine in the fracture, containing a large amount of salt but limited water, reduces water activity and slows evaporation. This rapid salt accumulation, up to 10 times the initial fracture mass, highlights the dominance of salt-induced capillary suction in quickly drawing surrounding brine into the fracture and suppressing matrix evaporation.

At medium and high flow rates, the mechanism is largely similar to that at low flow rates. The fracture initially loses brine due to partial displacement during injection, while evaporation from exposed fracture surfaces occurs. In the early stage, NaI in the fracture remains nearly constant, suggesting that evaporation is limited by slow vapor transport rather than brine movement, while capillary backflow from the matrix replenishes the fracture. As brine in the matrix begins to decrease due to stronger evaporation, the overall evaporation rate initially increases, but once matrix brine saturation drops further, evaporation slows and eventually ceases, as shown in Fig. 11. Upon entering the dry-out stage, the mass of salt in the fracture increases rapidly, primarily at the fracture-matrix interface, indicating that salt-induced capillary suction draws surrounding brine into the fracture and temporarily limits replenishment from the matrix. These observations demonstrate that higher gas flow accelerates drying, promotes rapid salt-induced capillary suction, and limits the time available for redistribution processes to counteract evaporation, highlighting the coupled roles of evaporation, capillary backflow, and salt precipitation in governing brine redistribution.

To further interpret these dynamics, the gas-liquid interfacial area was quantified as a function of water saturation (Fig. 12). At low flow rates, the interfacial area only slightly increases with a decrease in water saturation, consistent with capillary-dominated retention and limited evaporation. At medium and high flow rates, evaporation exceeds capillary replenishment, reducing matrix brine saturation and increasing interfacial area, which enhances evaporation until it reaches a maximum. Beyond this point, evaporation declines as capillary flow becomes insufficient. These findings indicate that evaporation is primarily controlled by the interplay between capillary flow and interfacial area, while also being modulated by wettability and capillary redistribution (Nasir et al., 2023).

Overall, the results indicate that the gas injection rate primarily affects the timing and spatial distribution of salt precipitation rather than altering the underlying mechanism. At low flow rates, evaporation proceeds more slowly due to the limited gas-liquid interfacial area, allowing the matrix to retain higher saturation for a longer period. This delays the onset of fracture precipitation but ultimately results in greater salt accumulation owing to prolonged capillary backflow. In contrast, high flow rates enhance evaporation in both the fracture and the matrix, leading to earlier salt precipitation. However, the rapid decline of matrix saturation limits the amount of salt transported to the fracture, resulting in relatively lower accumulation. Medium flow rates exhibit intermediate behavior, yet the fundamental two-stage process remains unchanged across all cases.

3.3 Salt accumulation effects on porous medium

In the following sections, we examine how this accumulation affects key properties of the porous medium, including salt pattern, porosity reduction, average pore size, and permeability. Fig. 13 presents pore-scale observations, confirming that salt precipitation occurs predominantly in the fracture zone at the normalized position $x/L = 0.5$ (observation window: $4.1 \times 2.8 \times 5.4$ mm^3). Fig. 14 illustrates the porosity reduction along the observed focus area for various flow rates.

At low flow rates, brine saturation within the fracture remains relatively low but retains isolated clusters. After 16 h of evaporation, saturation shrinking results in the formation of a characteristic “donut-shaped” meniscus between adjacent particles. This reflects the water-wet condition, where evaporation is the most intense particle contacts. By 38 h, brine distribution exhibits little change, with cluster locations and volumes remaining stable. After 52 h, partial refilling of the fracture occurs because previously isolated brine regions are reconnected owing to capillary backflow. At 81 and 124 h,

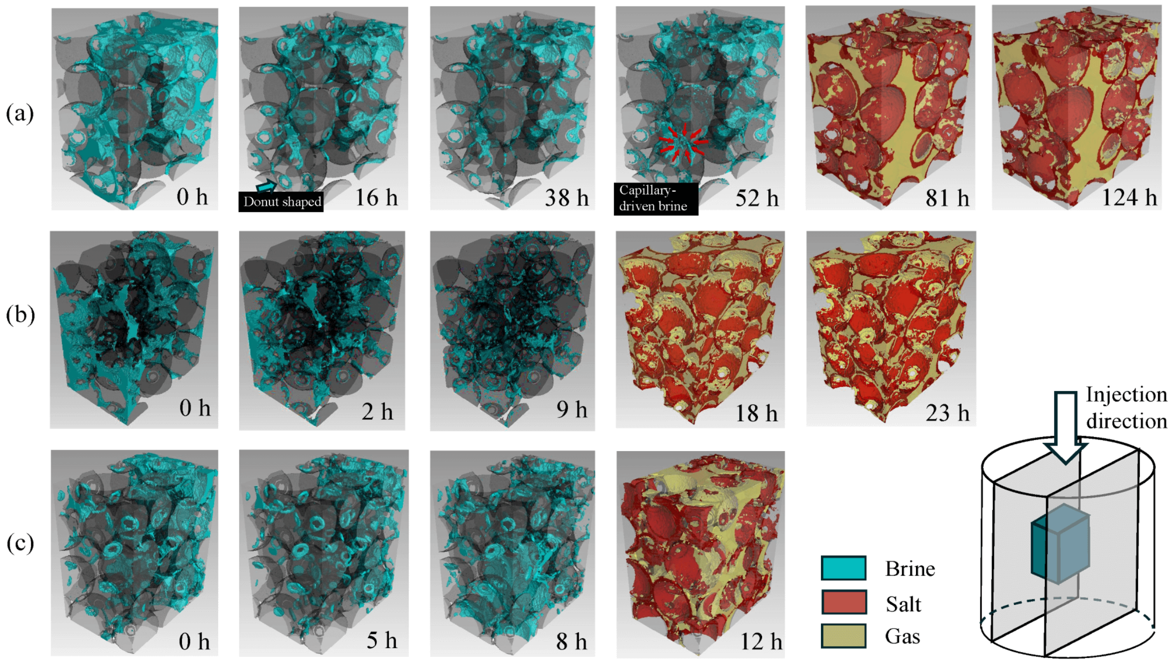

Fig. 13. Pore-scale visualization of the evaporation in the fracture region at flow rates of (a) 30, (b) 50, and (c) 80 cm^3/min. Cyan indicates brine below the solubility limit, whereas orange and yellow represent salt and gas, respectively, highlighting the brine morphology, capillary backflow, and gas pathways during dry-out.

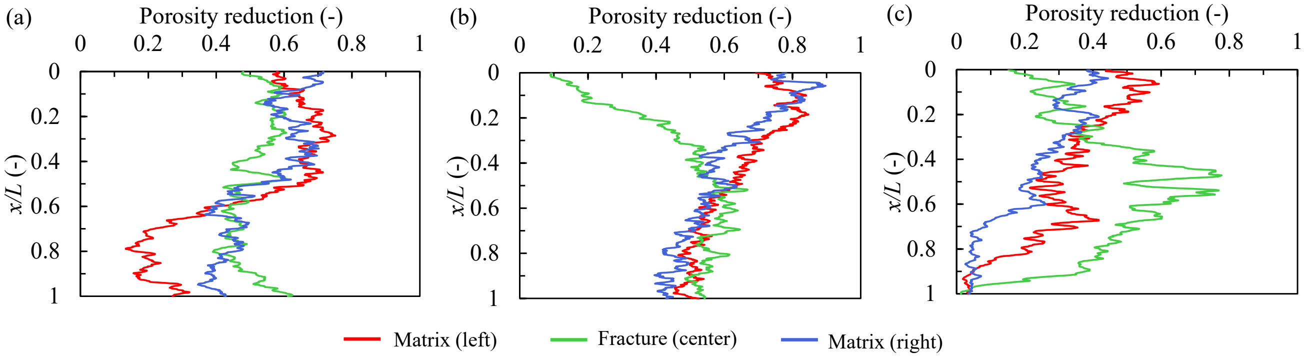

Fig. 14. Slice-averaged porosity reduction profiles for the matrix and fracture regions at flow rates of (a) 30, (b) 50, and (c) 80 cm^3/min under dry-out conditions.

salt precipitation nearly fills the fracture pores, with preferential accumulation at particle contacts because of water-wet behavior. The fracture porosity decreases uniformly by approximately 0.5 ± 0.1 for the entire length observation (Fig. 14(a)), although complete clogging is not observed.

At medium flow rates, the distribution pattern becomes more heterogeneous. In the fracture, less salt accumulates in the upper region ($x/L = 0.1$-0.5), where evaporation outpaces capillary replenishment. Meanwhile, the lower region ($x/L = 0.5$-1.0) remains nearly stagnant, maintaining a porosity reduction around 0.5. In the adjacent matrix, brine saturation gradually decreases from the top as evaporation proceeds, causing salt to concentrate in the upper zone. Over time, capillary backflow attempts to replenish the evaporated region, but prolonged evaporation drives salt accumulation near the top. Consequently, salt precipitation within the fracture becomes less pronounced near x/L = 0-0.4, where limited refilling occurs.

At high flow rates, evaporation dominates, and brine connectivity is strongly suppressed by viscous forces, resulting in lower overall salt deposition (Figs. 14(b) and 14(c)). The top and bottom portions of the fracture ($x/L = 0 - 0.4$) exhibit reduced salt accumulation owing to insufficient water replenishment, whereas the central region ($x/L = 0.6 - 0.8$) shows localized precipitation from surrounding brine. Salt deposition progressively narrows the pore throats, leading to a porosity reduction of approximately 0.4-0.5, which can be attributed to limited refilling in the upper region and fragmentation that restricts deposition in the lower region.

In summary, at low flow rates, abundant water supplied by longitudinal capillary flow produces nearly uniform salt deposition along the fracture. With increasing evaporation, water saturation near the fracture entrance decreases, leading to minimal deposition in this region. At the highest evaporation

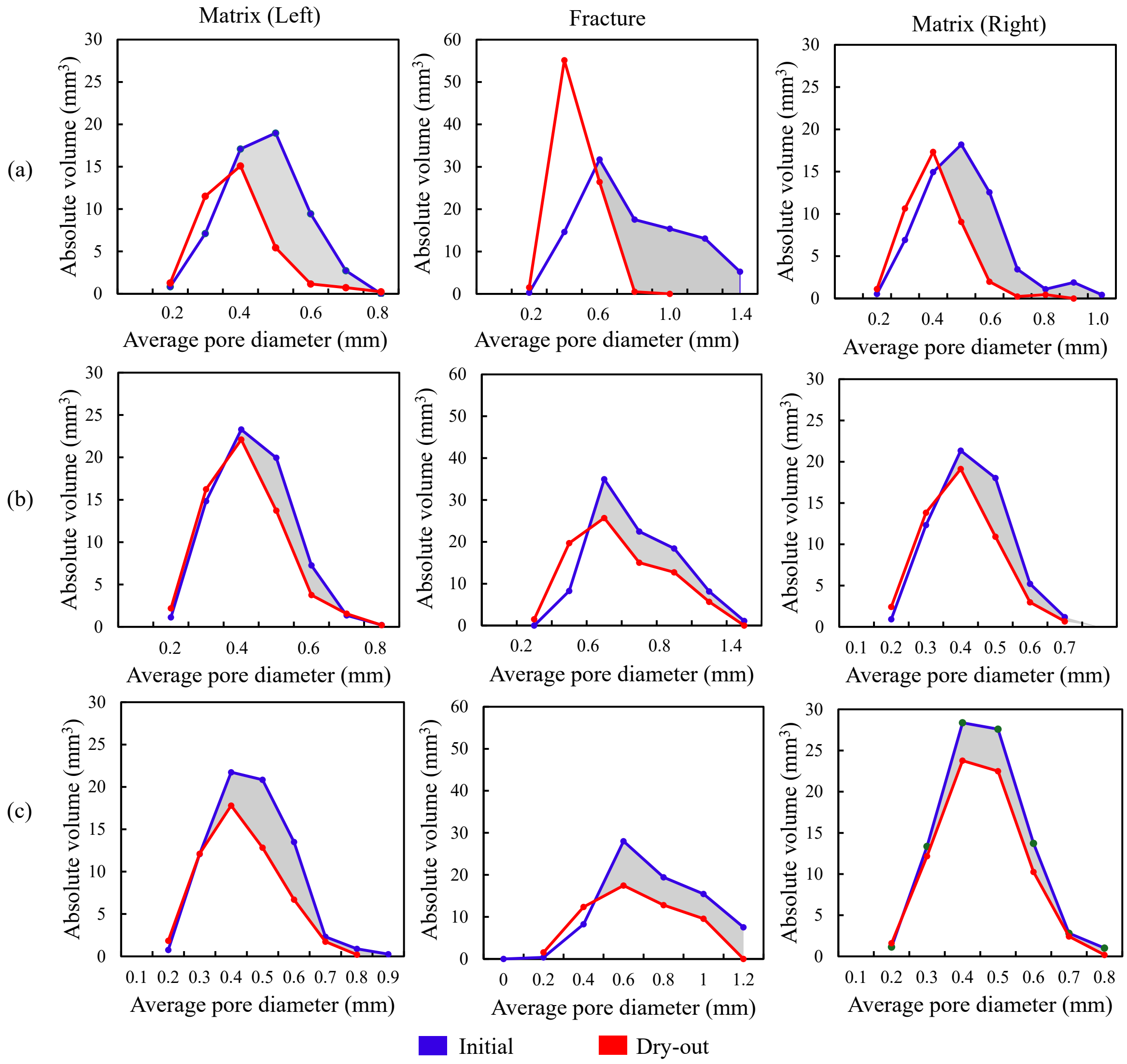

Fig. 15. Absolute pore volume as a function of average pore diameter for regions A-I, comparing the initial and dry-out conditions at flow rates of (a) 30, (b) 50, and (c) 80 cm^3/min. The gray shading highlights the volume reduction in larger pores.

rates, partial disconnection of water pathways further limits fracture replenishment, resulting in the lowest salt deposition in the lower region.

To assess how salt precipitation alters the pore structure under different gas injection conditions, pore-size reduction is analyzed across fracture and matrix regions by comparing absolute pore volume and pore-size distributions before and after precipitation. Fig. 15 shows the pore-size reduction caused by salt precipitation across different regions and flow rates, comparing absolute pore volume and pore-size distribution before and after precipitation. The results of pore-size distribution analysis (Fig. 15) reveal that increasing the CO_2 injection rate from 30 to 80 cm^3/min causes a shift in the dominant pore sizes and peak intensities. At the low flow rate of 30 cm^3/min (Fig. 15(a)), a distinct peak appears in the fracture region, whereas the matrix pores remain relatively stable indicating that salt preferentially migrates from matrix into the fracture and generates smaller pores. This reflects lateral transfer from matrix to fracture and localized clogging at particle contacts. At medium and high flow rates (Figs. 15(b) and 15(c)), the overall pore volume decreases, particularly in the larger-pore range, reflecting pore-interface narrowing due to salt accumulation and reduced connectivity.

The porosity reduction and changes in the average pore-size distribution in the fracture-matrix system are summarized in Table 3. Porosity loss in the fracture decreases as the flow rate increases, with the largest reduction occurring at the low flow rate (30 cm^3/min), while the highest flow rate (80 cm^3/min) yields a smaller porosity decrease. Conversely, the matrix shows relatively modest and spatially more uniform changes in pore geometry (average pore size ≈ 0.28 µm). We attribute these observations to the competing effects of evaporation intensity, capillary backflow and local clogging.

Using image-based Kozeny-Carman estimates that account for both porosity and pore-size changes, the effective intrinsic permeability in the observed volume was found to decrease

Table 3. Porosity reduction and altered average pore distribution in the matrix and fracture regions at three different flow rates.

Case	Injection rate (cm^3/min)	Porosity reduction (%)			Average pore-size reduction (%)		
		Matrix (left)	Fracture	Matrix (right)	Matrix (left)	Fracture	Matrix (right)
1	30	48	51	53	16	27	9
2	50	63	47	59	8	33	13
3	80	30	42	21	10	27	6

by 94%-95% in the fracture and by 55%-98% in the matrix, yielding an overall reduction of 55%-98% ($k/k_0 \approx 0.02$-0.45) across all flow conditions. The smallest reduction occurs at the highest flow rate, reflecting the lower volume of salt accumulation. Porosity reduction driven by mineral deposition supplied through capillary backflow, rather than pore shrinking alone, was considered the dominant mechanism of permeability loss. These findings indicate that salt precipitation during CO_2 injection can progressively impair reservoir injectivity, with the most severe impairment occurring under low- to medium-flow regimes where capillary backflow delivers the greatest brine volume into fractures.

4. Conclusions

Micro-CT was used to investigate the mechanisms of brine evaporation and salt precipitation in fractured porous media. Pore-scale mass transfer was assessed through measurements of brine saturation and concentration to quantify changes in water and salt mass within the fracture and matrix. We identified that the interplay between evaporation, capillary backflow, and salt precipitation governs salt accumulation, which occurs in two distinct stages.

In Stage I, gas created preferential pathways and partially displaced the brine. It preferentially invaded the larger pores in the fracture, resulting in low brine saturation and residual water films at particle menisci that sustained direct evaporation. During this stage, brine volume decreased but remained stable in the menisci and particle contact points due to due to high capillary pressure, while matrix pores remained fully saturated. Evaporation at the fracture-matrix interface was limited by the small interfacial area. Simultaneously, capillary forces replenished the evaporated water, maintaining brine availability and gradually increasing salt mass.

In Stage II, following the onset of salt precipitation in the fracture, salt-induced capillary suction drew surrounding water into the fracture, promoting further salt accumulation. The extent of precipitation toward the fracture center decreased with increasing gas flow rate. At low flow rates, capillary replenishment from the matrix dominated over evaporation, sustaining continuous brine supply and extensive salt deposition throughout the fracture. At high flow rates, evaporation prevailed, limiting brine transport and confining salt accumulation primarily to the fracture-matrix interface. Observed salt patterns confirmed the dominance of evaporation over capillary backflow within the fracture channel at all flow rates (Susanto et al., 2025). Salt primarily precipitated on particle surfaces, reducing effective pore sizes in both fracture and matrix and resulting in permeability reductions of up to 95% in the fracture zone.

This study elucidates and visualizes the mechanism of salt precipitation in fractured porous media by highlighting the dynamic interplay between evaporation, capillary backflow, and salt accumulation. Our findings demonstrate how gas flow rate directly regulates the balance between evaporation and brine replenishment from the matrix, determining both the extent and location of salt deposition within the fracture. These insights provide a predictive basis for mitigating wellbore clogging and managing the long-term integrity of fractured geological formations. Future research should examine the effects of capillary flow rate from the external reservoir to the matrix on overall salt precipitation patterns, offering a more complete, multi-scale understanding of the coupled processes.

Acknowledgements

This work was supported by the Japan Society for the Promotion of Science KAKENHI (Nos. 23K25024, 24H00441 and 25K07582), Japan Science and Technology Agency (JST) as part of Adopting Sustainable Partnerships for Innovative Research Ecosystem (ASPIRE) (No. JPMJAP2407), and the Department of Science and Technology of Jilin Province (No. 20230402077GH). The first author also acknowledges scholarship support from the TONEN International Scholarship Foundation.

Additional information: Author's email

matsushita.s.ad@m.titech.ac.jp (S. Matsushita);
suekane.t.aa@m.titech.ac.jp (T. Suekane).

Supplementary file

https://doi.org/10.46690/capi.2026.03.03

Conflicts of interest

The authors declare no competing interest.

References

Akindipe, D., Saraji, S., Piri, M. Salt precipitation during geological sequestration of supercritical CO_2 in saline aquifers: A pore-scale experimental investigation. Advances in Water Resources, 2021, 155: 104011.

Bachu, S. CO_2 storage in geological media: Role, means, status and barriers to deployment. Progress in Energy and Combustion Science, 2008, 34: 254-273.

Bernal, J. D., Mason, J. Packing of spheres: Co-ordination of randomly packed spheres. Nature, 1960, 188: 910-911.

Blunt, M. J. Multiphase Flow in Permeable Media: A Pore-Scale Perspective. Cambridge University Press, 2017.

Bogdanov, I. I., Mourzenko, V. V., Thovert, J. F., et al. Two-phase flow through fractured porous media. Physical Review E, 2003, 68: 026703.

Bultreys, T., Boone, M. A., Boone, M. N., et al. Fast laboratory-based micro-computed tomography for pore-scale research: Illustrative experiments and perspectives on the future. Advances in Water Resources, 2016, 95: 341-351.

Chen, X., Hu, R., Zhou, C., et al. Capillary-driven backflow during salt precipitation in a rough fracture. Water Resources Research, 2024, 60: 1-20.

Dashtian, H., Shokri, N., Sahimi, M. Pore-network model of evaporation-induced salt precipitation in porous media: The effect of correlations and heterogeneity. Advances in Water Resources, 2018, 112: 59-71.

Gostick, J. T. Versatile and efficient pore network extraction method using marker-based watershed segmentation. Physical Review E, 2017, 96: 023307.

Grimm Lima, M., Schädle, P., Green, C. P., et al. Permeability impairment and salt precipitation patterns during CO_2 injection into single natural brine-filled fractures. Water Resources Research, 2020, 56: e2020WR027213.

He, D., Jiang, P., Xu, R. Pore-scale experimental investigation of the effect of supercritical CO_2 injection rate and surface wettability on salt precipitation. Environmental Science & Technology, 2019, 53: 14744-14751.

Hu, Y., She, Y., Patmonoaji, A., et al. Effect of capillary number on morphological characterizations of trapped gas bubbles: Study by using micro-tomography. International Journal of Heat and Mass Transfer, 2020, 163: 120508.

Intergovernmental Panel on Climate Change (IPCC). Climate Change 2022: Mitigation of Climate Change (Sixth Assessment Report, AR6). Cambridge University Press, 2022.

Joekar-Niasar, V., Hassanizadeh, S. M. Analysis of fundamentals of two-phase flow in porous media using dynamic pore-network models: A review. Critical Reviews in Environmental Science and Technology, 2012, 42: 1895-1976.

Kézdi, Á. Soil Physics: Selected Topics. Amsterdam, Netherlands, Elsevier, 2013.

Miri, R., van Noort, R., Aagaard, P., et al. New insights on the physics of salt precipitation during injection of CO_2 into saline aquifers. International Journal of Greenhouse Gas Control, 2015, 43: 10-21.

Miri, R., Hellevang, H. Salt precipitation during CO_2 storage: A review. International Journal of Greenhouse Gas Control, 2016, 51: 136-147.

Nasir, M., Kaito, K., Patmonoaji, A., et al. Three-dimensional pore-scale observation of drying process of porous media. International Journal of Heat and Mass Transfer, 2022, 196: 123299.

Nasir, M., Li, Z., Mahardika, M. A., et al. Pore-scale investigation of wettability effects on drying process of three-dimensional porous medium. International Communications in Heat and Mass Transfer, 2023, 140: 106527.

Norouzi Rad, M., Shokri, N., Sahimi, M. Pore-scale dynamics of salt precipitation in drying porous media. Physical Review E, 2013, 88: 032404.

Ott, H., De Kloe, K. D., Marcelis, F., et al. Injection of supercritical CO_2 in brine-saturated sandstone: Pattern formation during salt precipitation. Energy Procedia, 2011, 4: 4425-4432.

Patmonoaji, A., Muharrik, M., Hu, Y., et al. Three-dimensional fingering structures in immiscible flow at the crossover from viscous to capillary fingering. International Journal of Multiphase Flow, 2020, 122: 103147.

Patmonoaji, A., Mahardika, M. A., Nasir, M., et al. Stereolithography 3D printer for micromodel fabrications with comprehensive accuracy evaluation by using microtomography. Geosciences, 2022, 12: 183.

Pruess, K., Müller, N. Formation dry-out from CO_2 injection into saline aquifers: Effects of solids precipitation and their mitigation. Water Resources Research, 2009, 45: W03402.

Raats, P. A. C. Dynamics of fluids in porous media. Soil Science Society of America Journal, 1973, 37: 206-208.

Roy, R. Evaporation-induced salt precipitation in porous media and the governing solute transport. West Lafayette, Purdue University, 2022.

Schindelin, J., Arganda-Carreras, I., Frise, E., et al. Fiji: An open-source platform for biological-image analysis. Nature Methods, 2012, 9: 676-682.

Seidell, A. Solubilities of inorganic and organic compounds. Agronomy Journal, 1928, 20: 1234-1245.

Shahidzadeh, N., Schut, M. F. L., Desarnaud, J., et al. Salt stains from evaporating droplets. Scientific Reports, 2015, 5: 10335.

Shahidzadeh-Bonn, N., Rafai, S., Bonn, D., et al. Salt crystallization during evaporation: Impact of interfacial properties. Langmuir, 2008, 24: 8599-8605.

Shokri, N. Pore-scale dynamics of salt transport and distribution in drying porous media. Physics of Fluids, 2014, 26: 012004.

Shokri, N., Lehmann, P., Or, D. Liquid-phase continuity and solute concentration dynamics during evaporation from porous media: Pore-scale processes near vaporization surface. Physical Review E, 2010, 81: 046308.

Sin, S., Imai, S., Mahardika, M. A., et al. Three-dimensional visualization of Rayleigh-Bénard convection in porous media. Advances in Water Resources, 2024, 186: 104666.

Suekane, T., Saito, Y., Jiang, L. Non-wetting phase saturation after drainage from the wetting-phase-filled porous medium. Journal of Fluid Science and Technology, 2015, 10: JFST0014.

Sun, L., Liu, Y., Ren, J., et al. Salt precipitation and pore structure changes during CO_2 injection into porous media. Journal of Cleaner Production, 2025, 505: 145446.

Susanto, W., Nasir, M., Mahardika, M. A., et al. Investigating the effects of flow rate on pore-scale mass transfer and salt spatial distribution in the drying process of porous media using X-ray microtomography. International Communications in Heat and Mass Transfer, 2025, 166: 109113.

Wang, G., Liu, Y., Xiong, W., et al. An improved non-local means filter for color image denoising. Optik, 2018, 173: 157-173.

Wu, H., Fang, C., Wu, R., et al. Drying of porous media by concurrent drainage and evaporation: A pore network modeling study. International Journal of Heat and Mass Transfer, 2020, 152: 118718.

Yan, L., Niftaliyev, R., Voskov, D., et al. Dynamics of salt precipitation at pore scale during CO_2 subsurface storage in saline aquifer. Journal of Colloid and Interface Science, 2025, 678: 419-430.

Zhang, D., Kang, Y., Selvadurai, A. P. S., et al. Experimental investigation of the effect of salt precipitation on the physical and mechanical properties of a tight sandstone. Rock Mechanics and Rock Engineering, 2020, 53: 4367-4380.

Zhang, S., Liu, H. Porosity-permeability relationships in modeling salt precipitation during CO_2 sequestration: Review of conceptual models and implementation in numerical simulations. International Journal of Greenhouse Gas Control, 2016, 52: 24-31.

Zhao, B., MacMinn, C. W., Juanes, R. Wettability control on multiphase flow in patterned microfluidics. Proceedings of the National Academy of Sciences of the United States of America, 2016, 113: 10251-10256.